

Electronic Supplementary Information for:

Radial alignment of c-channel nanorods in 3D porous TiO₂ for eliciting enhanced Li storage performance

Jayeon Baek,^{‡ab} Soomin Park,^{‡ab} Chyan Kyung Song,^{ab} Tae Yong Kim,^{ab} Inho Nam,^{ab} Jong
Min Lee,^a Jeong Woo Han^c and Jongheop Yi^{*ab}

^aSchool of Chemical and Biological Engineering, Seoul National University, Seoul 151-742,
Republic of Korea. E-mail: jyi@snu.ac.kr

^bWorld Class University (WCU) Program of Chemical Convergence for Energy &
Environment (C2E2), Institute of Chemical Processes, Seoul National University, Seoul 151-
742, Republic of Korea

^cDepartment of Chemical Engineering, University of Seoul, Seoul 130-743, Republic of
Korea.

[‡]J. B. and S. P. contributed equally to this work

Table of Contents

Experimental Section

● Preparation of TiO ₂ materials	S3
● Characterization	S3
● Electrochemical measurement	S3
● Computational details	S4

Supplementary Figures and Tables

● Fig. S1. Schematic illustrations of various rutile TiO ₂	S6
● Fig. S2. Possible Li migration pathways in rutile TiO ₂	S7
● Table S1. Diffusive characteristics of Li inside TiO ₂ nanorod	S8
● Fig. S3. Formation of a 3D-TS	S9
● Fig. S4. Controlling density of TiO ₂ nanorods	S11
● Fig. S5. Pore structure of the 3D-TS	S12
● Fig. S6. The atomic structures of TiO ₂ surfaces	S13
● Table S2. Calculated adsorption energy of Cl to TiO ₂ surface	S13
● Fig. S7. SEM images of TiO ₂ particles	S14
● Fig. S8. SEM, TEM images and XRD pattern of pc-TiO ₂ and nano-TiO ₂	S15
● Fig. S9. N ₂ adsorption-desorption isotherms of pc-TiO ₂ and nano-TiO ₂	S15
● Table S3. Quantified structural properties of TiO ₂	S16
● Fig. S10. Structural evolution of rutile TiO ₂ during (de)lithiation process	S17
● Fig. S11. First three charge/discharge voltage profiles of 3D-TS	S18
● Fig. S12. Charge/discharge voltage profiles at various C-rates	S19
● Fig. S13. SEM images of electrodes after 200 cycles	S20
● Table S4. Fitting parameters used to simulate EIS data	S21
● Fig. S14. Differential capacities	S22
● Fig. S15. Long cycle test	S23
● Fig. S16. The residual carbon contents in 3D-TS	S24
● Table S5. Yield of 3D-TS	S25

Abbreviations

- 3D-TS: three-dimensional and dendritic TiO₂ spherical structure
- nano-TiO₂: nano-sized and needle-like rutile TiO₂
- pc-TiO₂: micron-sized and polycrystalline TiO₂

Experimental Section

Preparation of TiO₂ materials

The synthesis of the 3D-TS was achieved in a bicontinuous emulsion phase formed from Winsor type III system. We used deionized water (D.I. water), cyclohexane, and magnesium stearate (Mg-stearate) for the Winsor type III ternary system composed of water, oil, and surfactant, respectively. First, 0.77 g of Mg-stearate (Riedel-de Haën) was dissolved in 30 ml of 2.6 M HCl (35~37%, Samchun) (Solution A). Titanium n-butoxide (4.06 ml, 97% purity, Aldrich) and 4.5 ml of n-amyl alcohol (99%, Samchun) were added to 30 ml of cyclohexane ($\geq 99\%$, Sigma-Aldrich) and the resulting solution was vigorously stirred for 20 min at room temperature (Solution B). Solutions A and B were mixed and additionally stirred for 30 min at room temperature. The mixture, composed of three different phases (oil-emulsion-water), was transferred into a 150 ml Teflon-sealed autoclave and maintained at 150 °C for 4 h. After cooling to room temperature, the reaction mixture was centrifuged and washed with ethanol three times (Fig. S16). The product was dried at 70 °C to obtain the final 3D-TS. In the synthetic process, about 90% of the titanium in the titanium n-butoxide is converted into TiO₂ in the 3D-TS (Table S5). Among the TiO₂ counterparts, micrometer-sized and poly-crystalline rutile TiO₂ particles (pc-TiO₂) were present, as has been previously reported.^{R1} Briefly, methanol, acetonitrile, water, dodecylamine, and titanium isopropoxide were mixed and used in hydrolysis and condensation reaction. The products were calcined in air at 700 °C for 4 h to obtain the final pc-TiO₂. The nanometer-sized, single-crystalline rutile TiO₂ particles were obtained from commercially available products (nano-TiO₂, Tayca, MT-100AQ).

(R1) S. Tanaka, D. Nogami, N. Tsuda and Y. Miyake, *J. Colloid Interface Sci.*, 2009, **334**, 188.

Characterization

The surface morphology of the samples was characterized by scanning electron microscopy (SEM, Carl Zeiss, SUPRA 55VP). An X-ray diffractometer (XRD, Rigaku, D/max-2200) was utilized to investigate crystalline structure of the TiO₂ samples. Bright-field transmission electron microscope (TEM) images and selected-area electron diffraction (SAED) pattern were collected by analytical TEM (JEOL, JEM-2100F). Nitrogen adsorption and desorption isotherm were measured using ASAP 2010 Micromeritics apparatus.

Electrochemical measurements

Electrochemical experiments were performed using a conventional coin cell (CR2032) assembled in an Ar-filled glove box. A lithium foil and microporous polypropylenes were used as the counter electrode and separator, respectively. The working electrode was prepared by mixing 80% w/w of the TiO₂ active materials, 10% w/w conductive carbon (Super P) and 10% w/w poly(vinylidene difluoride) binder for Li ion cells. The mixture was blended with a

few drops of N-methyl-2-pyrrolidone (NMP, Sigma-Aldrich) to produce slurry. The resulting slurries were casted on Cu foils by doctor blading and vacuum-dried at 120 °C for 12 h. After roller compression, film-type electrodes were obtained. A 1.15 M LiPF₆ solution of dissolved in 3:5:2 (v/v/v) ethylene carbonate/ethyl-methyl carbonate/diethyl carbonate were adopted as an electrolyte. Galvanostatic charge/discharge analyses were performed with an automatic battery cyler (WBCS3000, Wonatech) at ambient temperature (30 °C). Electrochemical impedance spectroscopy (EIS) was conducted using a computer-controlled potentiostat (ZIVE SP2, WonaTech) at E=1.85 V after 30 charge/discharge cycles. The frequency range was 10 mHz ~ 100 kHz under AC stimulus with a 10 mV amplitude. The parameters of the equivalent circuit were calculated by using ZMAN software.

Computational details

Periodic density functional theory (DFT) calculations were carried out using the Vienna ab initio simulation package (VASP).^{R2} We employed the generalized gradient approximation (GGA) parameterized by Perdew-Burke-Ernzerhof (PBE) exchange-correlation functional.^{R3} Ionic cores were described by the projector augmented wave (PAW) method.^{R4} The wave functions were constructed from the expansion of planewaves with an energy cutoff 400 eV. A 3 × 3 × 3 Monkhorst-Pack k-point mesh was used to sample the Brillouin zone. All calculations were converged until the forces on all atoms were less than 0.03 eV Å⁻¹. The electronic optimization steps were converged self-consistently to <10⁻⁶ eV. DFT+U within Dudarev's approach was used with U_{eff} = 4.2 to account for the on-site Coulomb interaction in the localized *d* orbital.^{R5} This U value has been obtained by fitting to experimental data the splitting between occupied and unoccupied Ti *d* states for oxygen vacancy states at the (110) surface of rutile TiO₂.^{R6} and has been used to model oxygen vacancies at other rutile surfaces^{R7}, Nb and Ta substitution^{R8}, and oxygen vacancy and Ti interstitial formation in rutile and anatase TiO₂.^{R9} For the calculation of bulk optimization, the cutoff energy was increased to 520 eV. The surface was constructed by cleaving the optimized bulk structure along the (001) and (110) surfaces. To prevent in-physical electronic interactions, a 10 Å of vacuum region space between the slabs was added. Both (001) and (110) surfaces largely consisted of 3 layers and the top 2 layers were allowed to relax while the residual bottom layer was fixed. The transition state was located using the climbing image-nudged elastic band (CI-NEB) method.^{R10} Seven spaced images were obtained by linear interpolation and used as initial trajectories for migration path. In the CI-NEB calculations, the images were refined until the maximum atomic forces are converged within 0.1 eV Å⁻¹. The difference in charge densities during Li migration was calculated using following equation: $\Delta\rho = \rho_{\text{LiTiO}} - (\rho_{\text{TiO}} + \rho_{\text{Li}})$ where ρ_{LiTiO} is the total charge density of the LiTiO system, ρ_{TiO} and ρ_{Li} are the charge densities of the TiO systems without Li and isolated Li atom, respectively.^{R11}

(R2) G. Kresse and J. Furthmüller, *Phys. Rev. B*, 1996, **54**, 11169.

(R3) J. P. Perdew, K. Burke and M. Ernzerhof, *Phys. Rev. Lett.*, 1996, **77**, 3865.

- (R4) P. E. Blöchl, *Phys. Rev. B*, 1994, **50**, 17953.
- (R5) S. L. Dudarev, G. A. Botton, S. Y. Savrasov, C. J. Humphreys and A. P. Sutton, *Phys. Rev. B*, 1998, **57**, 1505; U. Aschauer and A. Selloni, *Phys. Chem. Chem. Phys.*, 2012, **14**, 16595.
- (R6) B. J. Morgan and G. W. Watson, *Surf. Sci.*, 2007, **601**, 5034.
- (R7) B. J. Morgan and G. W. Watson, *J. Phys. Chem. C*, 2009, **113**, 7322.
- (R8) B. J. Morgan, D. O. Scanlon and G. W. Watson, *J. Mater. Chem.*, 2009, **19**, 5175.
- (R9) B. J. Morgan and G. W. Watson, *J. Phys. Chem. C*, 2010, **114**, 2321.
- (R10) G. Henkelman, B. P. Uberuaga and H. A. Jónsson, *J. Chem. Phys.*, 2000, **113**, 9901; G. Henkelman and H. Jónsson, *J. Chem. Phys.*, 2000, **113**, 9978.
- (R11) Y. S. Yun, K. R. Lee, H. Park, T. Y. Kim, D. Yun, J. Han and J. Yi, *ACS Catal.*, 2015, **5**, 82; J. Kang, A. Hirata, L. Kang, X. Zhang, Y. Hou, L. Chen, C. Li, T. Fujita, K. Akagi and M. Chen, *Angew. Chem., Int. Ed.*, 2013, **52**, 1664.

Supplementary Figures and Tables

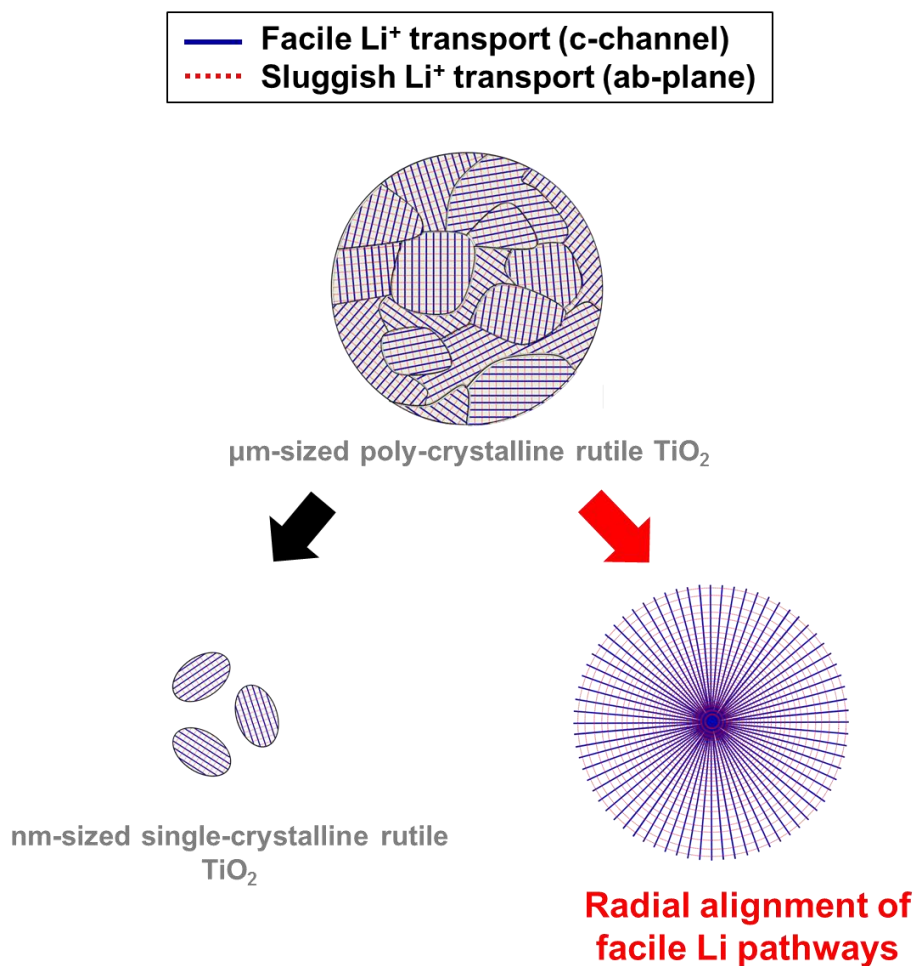


Fig. S1. Schematic illustration showing the various architectures of rutile TiO₂

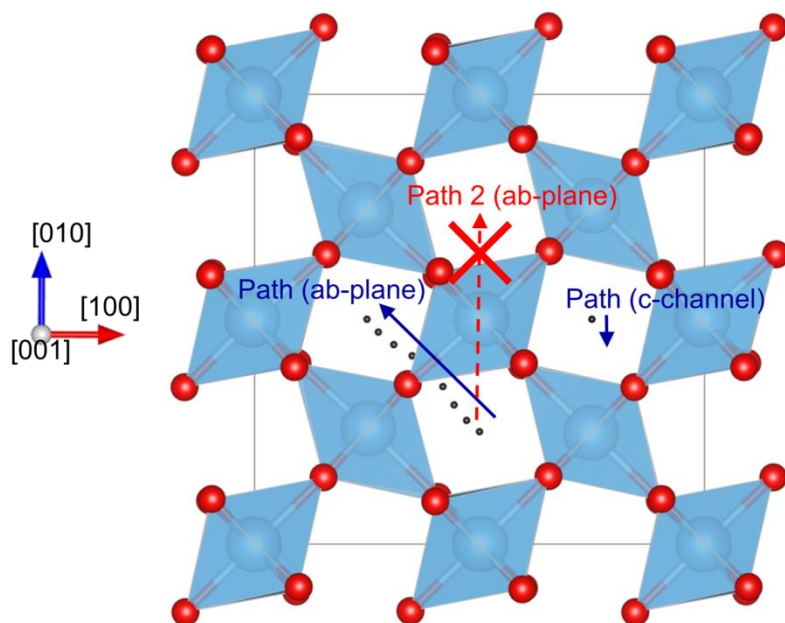
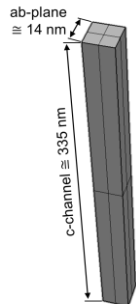


Fig. S2. Possible Li migration pathways in rutile TiO_2 . The path (c-channel) represents Li migration along a c-axis, and path (ab-plane) corresponds to the movement of Li to the nearest neighbor diagonal channel in the $[110]$ direction. Path 2 (ab-plane) corresponds to Li migration in the $[010]$ direction directly through edge-sharing octahedrons, which is not a feasible pathway due to the tremendous energy barrier.

Table S1. Diffusion characteristics of Li inside TiO₂ nanorod with specialized c-channels.

	Migration distance (<i>d</i>)	Energy barrier (<i>E_{act}</i>)	Diffusivity at 305K ^(a) (<i>D</i>)	Geometry of nanorod	Time constant ^(b) (<i>τ_d</i>)
Unit	Å	eV	cm ² s ⁻¹		s
c-channel	3.32	0.05	1.64×10 ⁻³		6.84×10 ⁻⁷
ab-plane	3.03	1.83	5.30×10 ⁻³³		3.70×10 ²⁰

Note. In DFT calculations, a Li_{0.06}TiO₂ crystal model was used to evaluate the energy barrier.

^{a)} Diffusivity was calculated using the Einstein-Smoluchowski relation: $D = g\Gamma d^2$

where $g (\cong 1)$ is a geometric factor, $\Gamma (= \nu^* \exp \frac{-E_{act}}{k_B T})$ is the hopping frequency between sites ($\nu^* \cong 10^{13}$) and d is migration distance.

^{b)} $\tau_d = \frac{L^2}{D}$

Detailed description on the diffusion of Li inside the 3D-TS

DFT-calculated migration energy barriers (*E_{act}*)/distances (*d*) were converted to Li diffusivities (*D*) using the Einstein-Smoluchowski relation. The *D* for the c-channel pathway was approximated to be 10⁻³ (cm² s⁻¹) at a temperature of 305K, which implies that the c-channel can be a very rapid Li diffusion pathway surpassing other related electrode materials.^{R12} By contrast, Li transport through the ab-plane pathway is very sluggish (*D*=10⁻³³~10⁻³² cm² s⁻¹). Considering the geometry of TiO₂ nanorods (approximately 335 nm×14 nm in [001] and [110] directions, respectively), the diffusion time is only $\tau_d = 10^{-4} \sim 10^{-3}$ ms, which is much less than the shortest reported charge/discharge time of 10 s.^{R13} Despite its short length, the ab-plane pathway shows a tremendous time constant of around 10²⁰ seconds. Although diffusion in single nanorods cannot be elucidated experimentally, even with *D*=10⁻⁹~10⁻¹⁰ cm² s⁻¹ from a previous study,^{R14} the diffusion time for a 300 nm nanorod is only 16 ms. Therefore, it is reasonable to consider that the 3D-TS containing elongated c-channel is sufficient to transport Li through bulk crystals even during rapid charge/discharge operations.

(R12) P. He, X. Zhang, Y. –G. Wang, L. Cheng and Y. –Y. Xia, *J. Electrochem. Soc.*, 2008, **155**(2), A144; J. –G. Kim, M. –S. Park, S. M. Hwang, Y. –U. Heo, T. Liao, Z. Sun, J. H. Park, K. J. Kim, G. Jeong, Y. –J. Kim, J. H. Kim and S. X. Dou, *ChemSusChem*, 2014, **7**, 1451; B. Ziebarth, M. Klinsmann, T. Eckl and C. Elsässer, *Phys. Rev. B*, 2014, **89**, 174301.

(R13) B. Kang and G. Ceder, *Nature*, 2009, **458**, 190.

(R14) S. Bach, J. P. Pereira-Ramos and P. Willman, *Electrochim. Acta*, 2010, **55**, 4952.

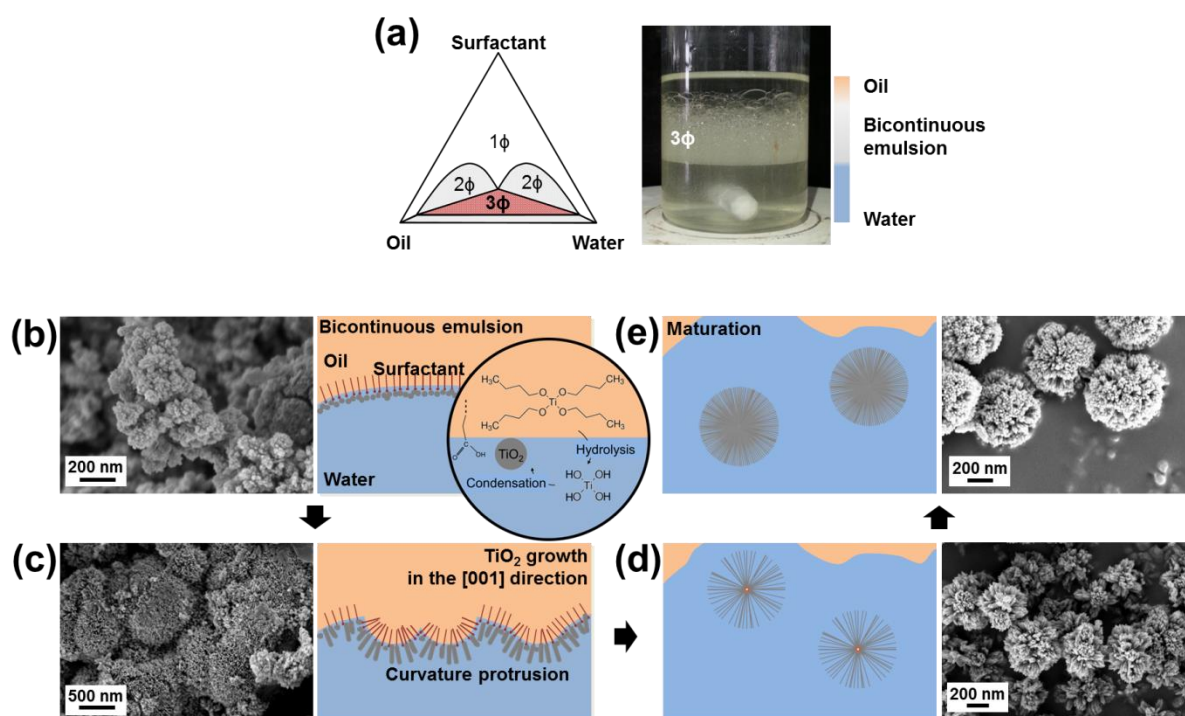


Fig. S3. (a) Phase behavior of the Winsor III system (left). The term “ $n\phi$ ” indicates the number of phases, and 3ϕ indicates bicontinuous emulsion phase. Optical image and schematic of Winsor III system (right). (b-e) Schematic illustrations and corresponding SEM images of reaction intermediates of 3D-TS as a function of time (0.5, 1, 2, and 4 h).

Detailed description on the formation of a 3D-TS

At the initial stage of the reaction (Fig. S3b), the titanium n-butoxide is located in the oil phase (cyclohexane) due to the hydrophobic nature of the tert-butoxide ligands ((O-C₄H₉)₄)^{R15}. The surfactant (Mg-stearate) exists at the oil/water interface, and this eventually leads to the formation of a bicontinuous emulsion phase (3ϕ) when the desired amounts of water, oil, and surfactant are mixed. The titanium n-butoxide in cyclohexane is steadily hydrolyzed and the products pass into the water phase and the condensation reaction of titanium hydroxide ($\text{Ti}(\text{OH})_4 \rightarrow \text{TiO}_2$) follows. During the condensation reaction to TiO_2 , the high acidity of the water phase (2.6 M of HCl) leads to edge-shared linking and corner-shared bonding of the $[\text{TiO}_6]$ octahedron, which results in the formation of the rutile phase of TiO_2 .^{R16} The $[\text{TiO}_6]$ octahedrons are linked by sharing two opposite edges to form chains along the c-axis, which is closely related to the c-channel, namely ‘Li highway’. After this series of sequential reactions, primary rutile nanocrystallites are produced, as evidenced by the SEM image of Fig. S3b.

After the formation of primary TiO_2 nanoparticles, the secondary crystal growth begins (Fig. S3c). During the secondary crystal growth of TiO_2 , the generation of curvatures (denoted in Fig. S3c) at the oil/water interface is important for determining the spherical shape of the 3D-TS. The driving force for the generation of curvature is a tendency to maintain a charge balance at the oil/water interface. The hydrolyzed titanium hydroxides (in the acidic water

phase) that have a positive charge and head-groups of the anionic surfactant are stably bound and neutralized by Coulomb interactions. As the titanium hydroxides are converted into non-ionizing TiO₂ during the condensation reaction, the TiO₂ rods that are compressed together to sustain charge balance. In this situation, the interfacial area between the oil and water, where the head-group of the surfactant is located, are continuously increased, and the curvatures begin to protrude. In the end, the protruded curvatures form a closed structure with a spherical morphology.^{R17} Fig. S3c and S3d display schematic illustrations and corresponding SEM images explain the extrusive evolution.

The assembly of TiO₂ nanorods separated from the oil/water interface undergoes a maturation process (Fig. S3e). In the process, the titanium hydroxides in water phase are continually accessible to the TiO₂ assembly for the construction of fresh TiO₂ rods and to prolong pre-existing TiO₂ rods. This maturation process allows the overall surface energy to be minimized.

(R15) Z. Shan, E. Gianotti, J. C. Jansen, J. A. Peters, L. Marchese and T. Maschmeyer, *Chem. - Eur. J.*, 2001, **7**, 1437.

(R16) T. -D. N. Phan, H. -D. Pham, T. V. Cuong, E. J. Kim, S. Kim and E. W. Shin, *J. Cryst. Growth*, 2009, **312**, 79.

(R17) A. Monnier, F. Schüth, Q. Huo, D. Kumar, D. Margolese, R. S. Maxwell, G. D. Stucky, M. Krishnamurty, P. Petroff, A. Firouzi, M. Janicke and B. F. Chmelka, *Science*, 1993, **261**, 1299.

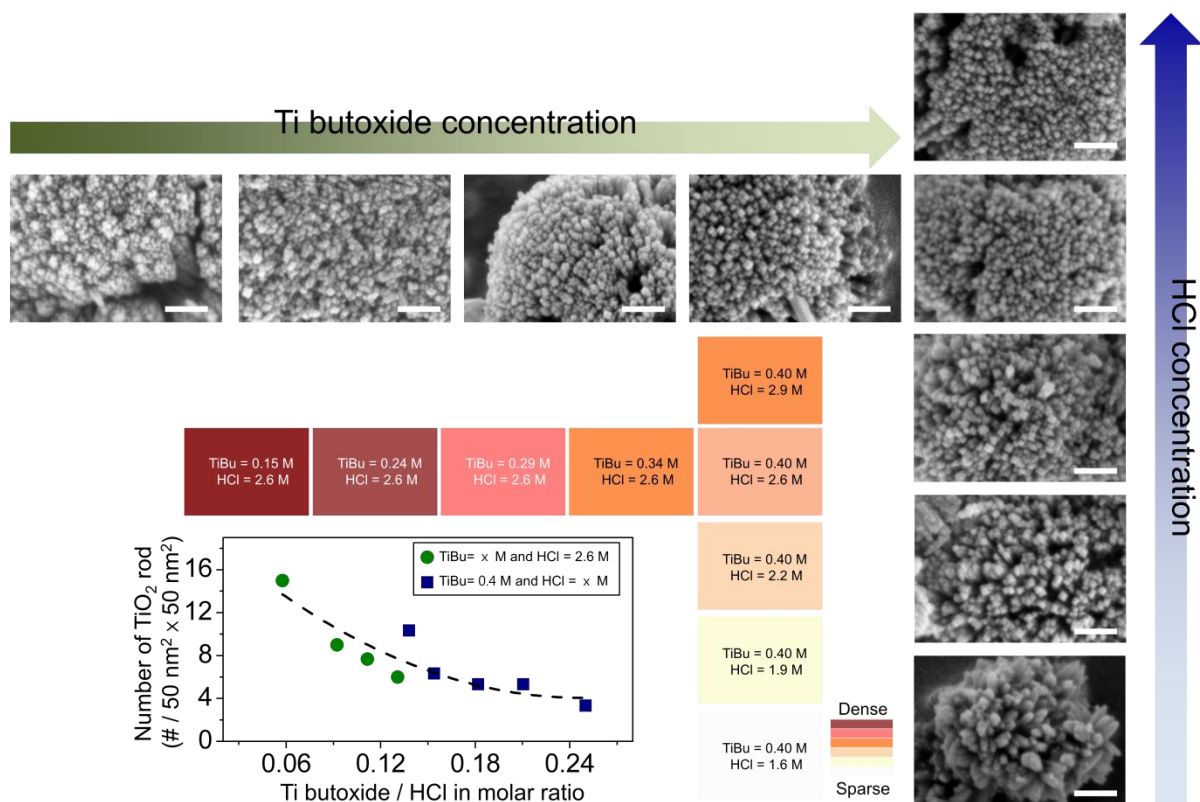


Fig. S4. Controlling the density of TiO₂ nanorods. SEM images in equal scale of 3D-TS synthesized under the various Ti butoxide/HCl molar ratios (scale bar = 100 nm).

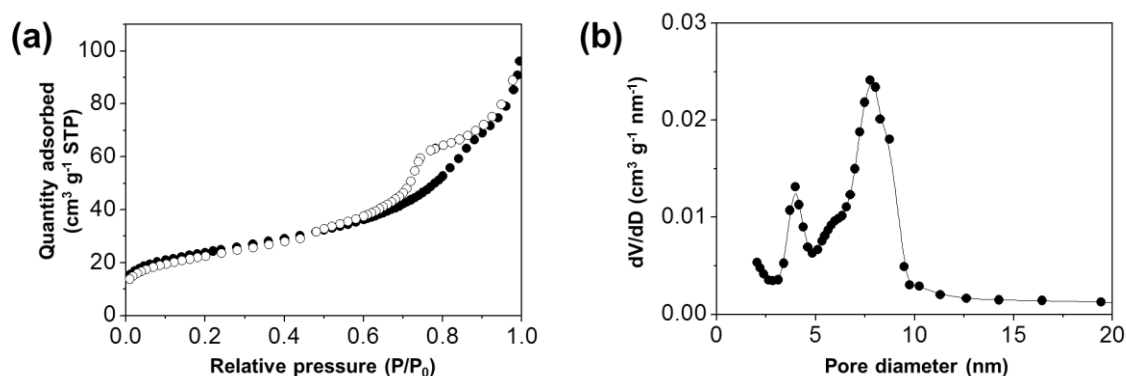


Fig. S5. (a) Nitrogen adsorption-desorption isotherms and (b) pore size distribution curves of 3D-TS.

Detailed description on the porous structure of the 3D-TS

The 3D-TS exhibited a type IV isotherm with a H2 type hysteresis loop in the relative pressure range of 0.6 ~ 1.0, indicating the existence of various sized mesopores (Fig. S5a).^{R18} The pore size distribution (Fig. S5b, calculated from the desorption branch using the Barrett-Joyner-Halenda method) confirms the multimodal pore size distribution, which consists of a relatively sharp peak (4 nm), a feeble shoulder peak (6 nm), and a broad peak (8 nm). This distribution arises from the interior space of hierarchical structure containing radially assembled TiO₂ nanorods. The overall surface area (calculated using the Brunauer-Emmett-Teller theory) is ~82.9 m² g⁻¹. Quantified properties are summarized in Table S2.

(R18) K. S. W. Sing, D. H. Everett, R. A. W. Haul, L. Moscou, R. A. Pierotti, J. Rouquérol and T. Siemieniewska, *Pure Appl. Chem.*, 1985, **57**, 603.

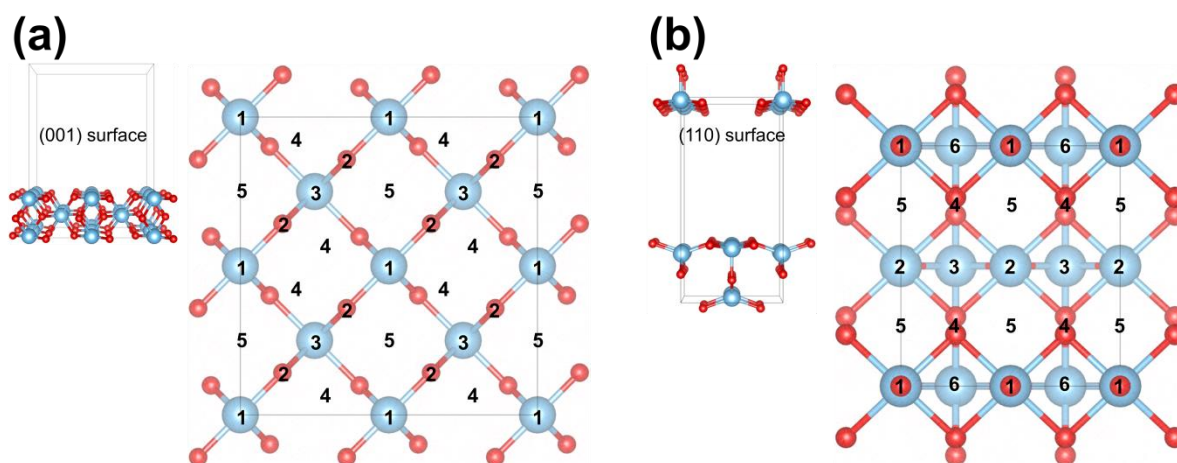


Fig. S6. The atomic structures of TiO_2 surfaces. A hexahedron represents the boundary of a primitive unit cell (left images of a and b, respectively) and the adsorption positions of chlorine are denoted (right images of a and b, respectively).

Table S2. Calculated results of the adsorption energy of Cl to the TiO_2 surface. The adsorption positions (#1 ~ #6) are shown in Fig. S6.

Parameter	Adsorption energy of Cl to TiO_2 surface (eV)	
	(001) Surface	(110) Surface
$E_{\text{ads}}^{\text{a)}} (1)$	-2.31	-4.27
$E_{\text{ads}} (2)$	-1.47	-3.14
$E_{\text{ads}} (3)$	-0.77	-2.83
$E_{\text{ads}} (4)$	-2.30	-2.99
$E_{\text{ads}} (5)$	-1.43	-3.37
$E_{\text{ads}} (6)$	-	-3.58
Total energy of single Cl atom ^{b)}	-0.26	-0.26
Total energy of TiO_2 surface	-260.18	-150.29

^{a)} Adsorption energy of Cl at \times position ($E_{\text{ads}}(\times) = E_{\text{Cl-surface}} - E_{\text{Cl}} - E_{\text{surface}}$); ^{b)} Single Cl atom is placed in $10 \times 10 \times 10 \text{ \AA}^3$ unit cell.

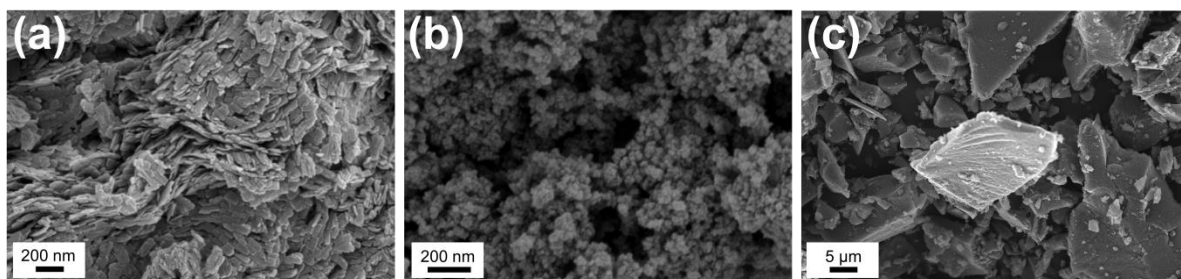


Fig. S7. SEM images of TiO₂ particles synthesized using dilute, aqueous solutions of H₃PO₄ (a), HNO₃ (b), and CH₃COOH (c). Other synthesis conditions including oil, co-solvent, and surfactant remain unchanged.

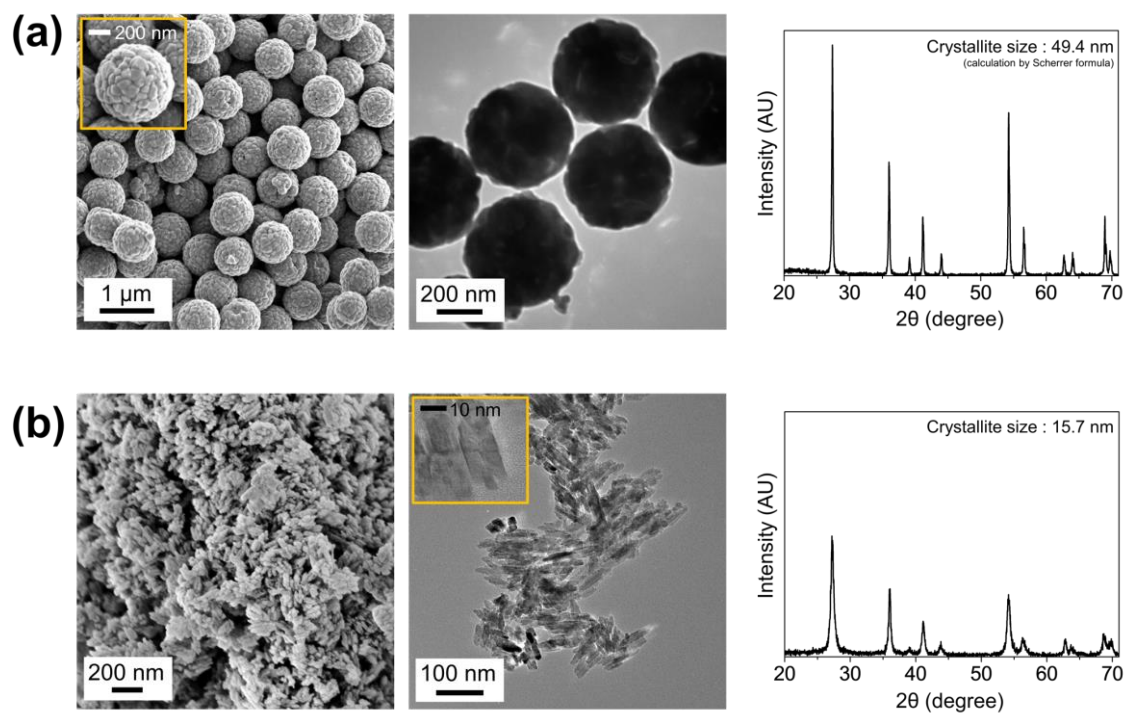


Fig. S8. SEM, TEM images and XRD pattern of rutile (a) pc-TiO₂ and (b) nano-TiO₂ particles, respectively.

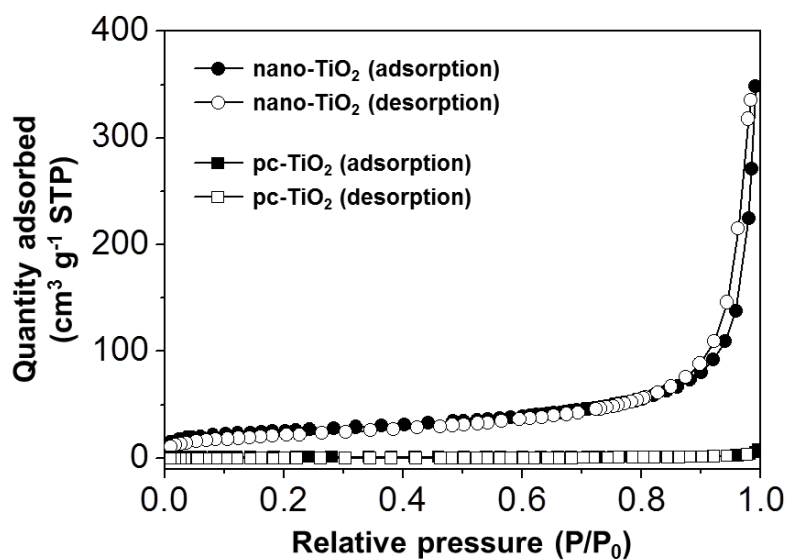


Fig. S9. Nitrogen adsorption-desorption isotherms of nano-TiO₂ and pc-TiO₂.

Table S3. Quantified structural properties of TiO₂.

Parameter	BET surface area		Average pore diameter	Total pore volume
	Unit	m ² g ⁻¹	nm	cm ³ g ⁻¹
3D-TS		82.9	6.19	0.132
nano-TiO ₂		89.6	18.9	0.348
pc-TiO ₂		3.39	36.1	0.006

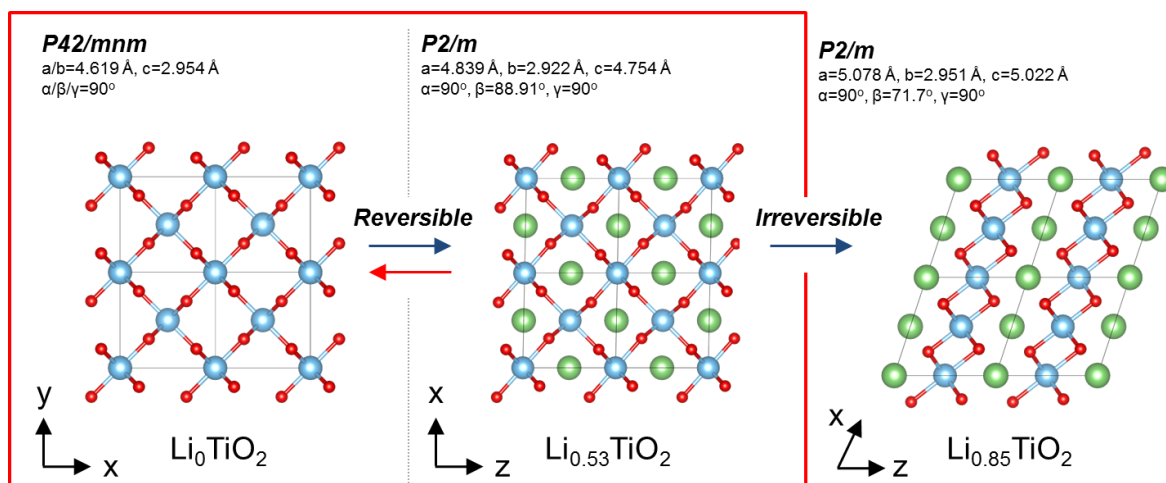


Fig. S10. Structural evolution of rutile TiO_2 during (de)lithiation process. The lithiation of TiO_2 up to $\text{Li}/\text{Ti}=0.53$ resulted in a phase transition toward an intermediated phase, very similar to the original rutile phase but slightly deformed, thus reducing the symmetry to the monoclinic $P2/m$ space group.^{R19} This reversible phase transformation between TiO_2 ($P42/mnm$) and $\text{Li}_{0.53}\text{TiO}_2$ ($P2/m$) is mainly responsible for creating the noticeable plateau-like regions with centers at 1.85 V. Importantly, the transformation to $P2/m$ $\text{Li}_{0.53}\text{TiO}_2$ is achieved by Li insertion migrating through the c-channel pathway and subsequent deformation of the original $P42/mnm$ TiO_2 . For this reason, the 3D-TS showed a capacity of 190 mAh g^{-1} (at 0.2C, 10th cycle) and the corresponding composition of $\text{Li}_{0.57}\text{TiO}_2$ which is similar Li/Ti ratio of $\text{Li}_{0.53}\text{TiO}_2$.

(R19) W. J. H. Borghols, M. Wagemaker, U. Lafont, E. M. Kelder and F. M. Mulder, *Chem. Mater.*, 2008, **20**, 2949.

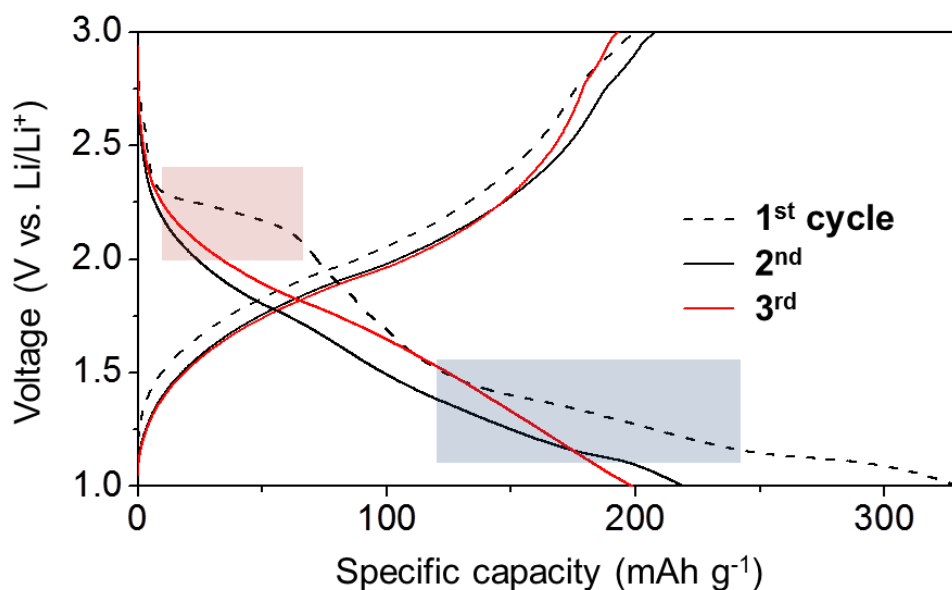


Fig. S11. First three charge/discharge voltage profiles of 3D-TS at a rate of 0.2C. In the 1st lithiation process, two distinct potential plateaus appear at 2.2 (red shadow) and 1.4 V (blue shadow). The potential plateau at 1.4 V is commonly found in rutile TiO₂, and has also been reported in the literatures.^{R20} However, the profile containing plateau at 2.2 V is not consistent with that of other TiO₂ reported previously, and the plateau disappears after 1st cycle. We concluded that this unknown plateau originated from the organic impurities and that are completely decomposed under the oxidative conditions. In fact, CHNS analysis results (carbon content of 2.05 wt. %) revealed the presence of trace amounts of residual surfactants and butyl groups. Even if the 60 mAh g⁻¹ from the 2.2 V plateau were not related to the insertion of Li into TiO₂, the 3D-TS was able to accommodate Li up to Li_{0.8}TiO₂ (270 mAh g⁻¹) during the 1st lithiation process. Subsequently, 0.57 mol of Li per mol TiO₂ (Li_{0.57}TiO₂, 190 mAh g⁻¹) could be cycled reversibly. An irreversible loss in capacity (Li_{0.23}TiO₂) during the first charge/discharge was also observed for other TiO₂ polymorphs and nanosized rutile, which is attributed to the irreversible structural change (Li_{0.85}TiO₂ with *P2/m* space group) due to the deeper penetration of Li (1.0~1.4 V vs. Li/Li⁺).^{R21}

(R20) D. Wang, D. Choi, Z. Yang, V. V. Viswanathan, Z. Nie, C. Wang, Y. Song, J. -G. Zhang and J. Liu, *Chem. Mater.*, 2008, **20**, 3435; Y. -S. Hu, L. Kienle, Y. -G. Guo and J. Maier, *Adv. Mater.*, 2006, **18**, 1421.

(R21) E. Baudrin, S. Cassaignon, M. Koelsch, J. -P. Jolivet, L. Dupont and J. -M. Tarascon, *Electrochem. Commun.*, 2007, **9**, 337; H. Qiao, Y. Wang, L. Xiao and L. Zhang, *Electrochem. Commun.*, 2008, **10**, 1280.

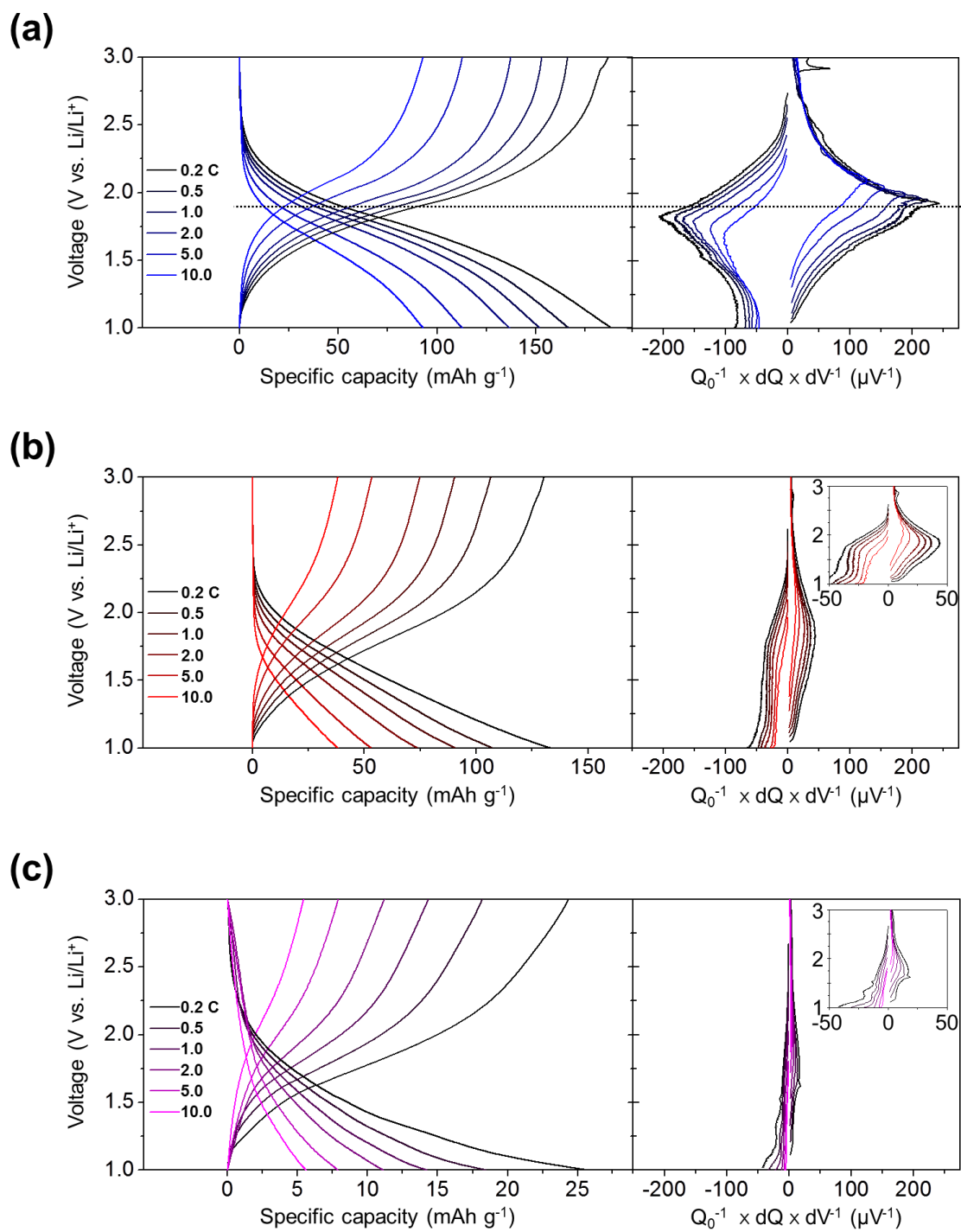


Fig. S12. Galvanostatic charge/discharge voltage profiles and corresponding differential capacities for (a) 3D-TS, (b) nano-TiO₂, and (c) pc-TiO₂ at various C-rates (0.2C ~ 10C).

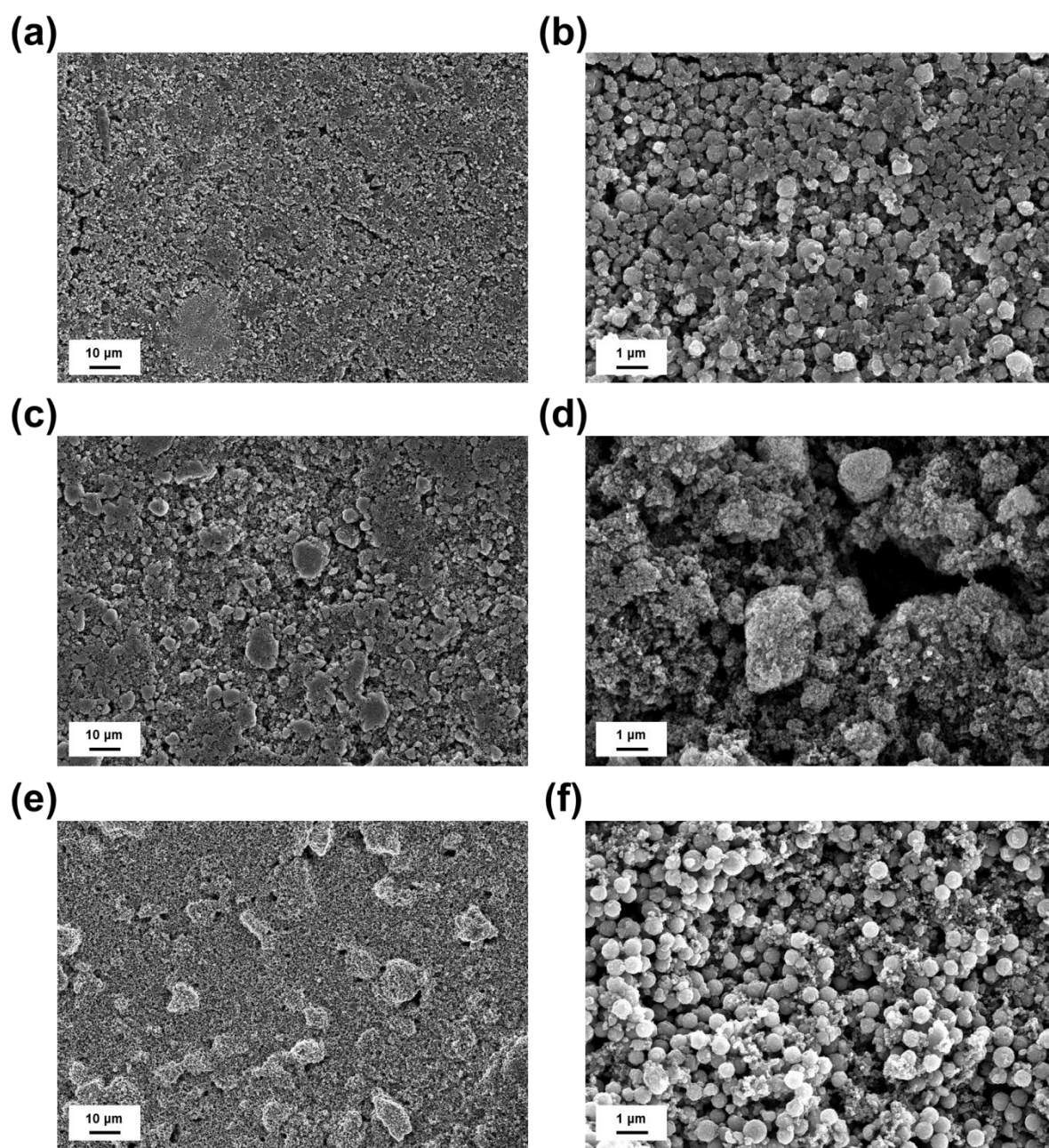


Fig. S13. SEM images of electrodes after 200 cycles; (a, b) 3D-TS, (c, d) nano-TiO₂, and (e, f) pc-TiO₂.

Table S4. Fitting parameters used to simulate the EIS data.

Parameter	Active material			
	Unit	3D-TS	nano-TiO ₂	pc-TiO ₂
R _e	Ω	4.76	3.74	3.67
R _{ct}	Ω	41.2	261	238
R _{ic}	Ω	39.3	354	305
A _W ^{a)}	mΩ s ^{-0.5}	0.037	0.387	1.01

$$^a) A_W = \frac{RT}{An^2 F^2 \theta C \sqrt{2D}}$$

where R is the gas constant, T is the temperature, A is the diffusion area, n is the valency, F is the Faraday constant, C is the concentration of Li⁺, D is the diffusion coefficient of Li in electrode and θ denotes the fraction of the reduced and oxidized species present.

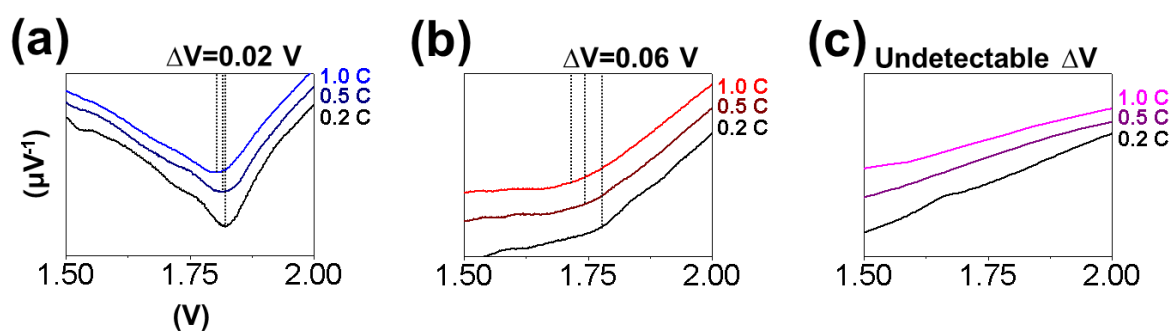
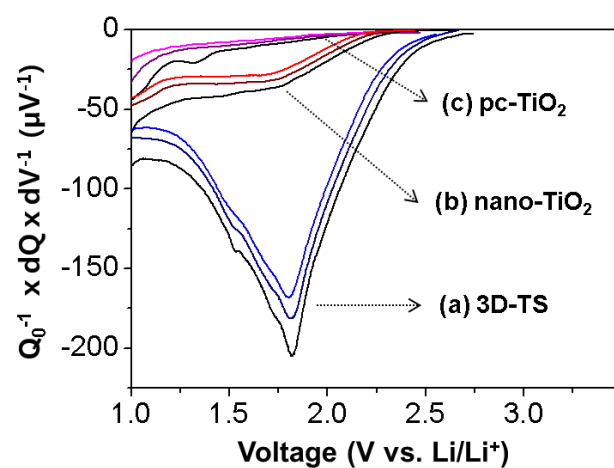


Fig. S14. Differential capacities (obtained from galvanostatic charge voltage profiles at 0.2, 0.5, and 1.0 C) of (a) 3D-TS, (b) nano-TiO₂, and (c) pc-TiO₂.

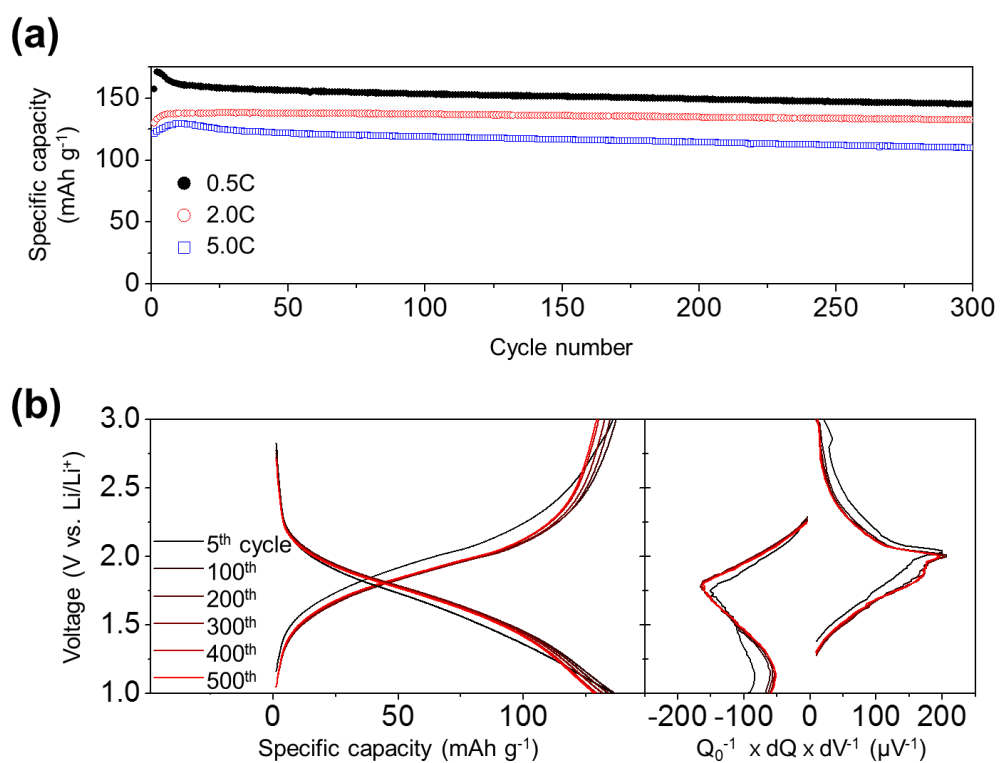


Fig. S15. (a) Discharge capacities of the 3D-TS at 0.5, 2.0, and 5.0C during galvanostatic cycles. (b) The evolution of voltage profiles and corresponding differential capacities of the 3D-TS during long cycles test at 2.0C.

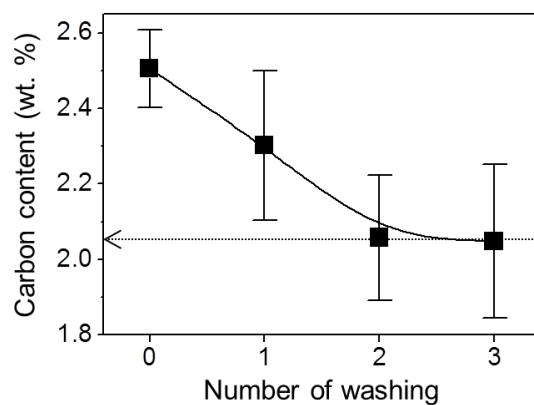


Fig. S16. The residual carbon contents as a function of washing times for 3D-TS. The identified carbon content of organic impurities were about 2.05 wt. %. An CHNS corder (TruSpec Micro CHNS) was utilized for elemental analyses.

Table S5. Yield of 3D-TS.

	Chemical	Quantity (g)	Ti content (g)	Note
Used	Titanium (IV) n-butoxide	3.94	0.554	-Reagent grade, 97% -Molecular weight 340.32 -Density 1.00 g ml ⁻¹
Produced	TiO ₂ (3D-TS)	0.839	0.503	-Molecular weight 79.87 -Exclusion of organic impurities
Ti conversion			90.8%	